Response of remanent magnetization to deformation in geological processes using 3D-printed structures

Journal Article

Author(s):
Liu, Pengfei; Gervasoni, Simone; Madonna, Claudio; Gu, Hongri; Coppo, Andrea; Pané, Salvador; Hirt, Ann Marie (iD)

Response of remanent magnetization to deformation in geological processes using 3D-printed structures

Pengfei Liu[1,2**], Simone Gervasoni[3**], Claudio Madonna[4], Hongri Gu[3], Andrea Coppo[3], Salvador Pané[3], Ann M. Hirt[1*]

1   Institute of Geophysics, ETH Zürich, Sonneggstrasse 5, CH-8092 Zürich, Switzerland

2   State Key Laboratory of Lunar and Planetary Sciences, Macau University of Science and Technology, Macau, P.R. China

3   Institute of Robotics and Intelligent Systems, ETH Zürich, Sonneggstrasse 5, CH-8092 Zürich, Switzerland

4   Geological Institute, ETH Zürich, Sonneggstrasse 5, CH-8092 Zürich, Switzerland

[*]Corresponding author: ann.hirt@erdw.ethz.ch (A. M. Hirt)

[**]Shared first author

Email: pengfei.liu2018@outlook.com (P. Liu), gesimone@student.ethz.ch (S. Gervasoni), claudio.madonna@erdw.ethz.ch (C. Madonna), hgu@student.ethz.ch (H. Gu), andrea.coppo@gmail.com (A. Coppo), vidalp@ethz.ch (S. Pané), ann.hirt@erdw.ethz.ch (A. M. Hirt),

Abstract

Palaeogeographic reconstructions and construction of apparent polar wander paths are dependent on having reliable palaeomagnetic directions. The importance of inclination flattening in biasing the palaeomagnetic record has been debated for over 60 yrs. Correction for this effect often assumes that the palaeomagnetic vector deforms as a passive line. In a novel approach using 3D printed analogue rocks, we revisit the question of how a palaeomagnetic vector responds to deformation, specifically compaction. Maghaemite nanoparticles were mixed in the printing resin with a concentration of 0.15 wt. %, and five series of cylinders with 1 cm height and diameter were printed with porosities between 0% and 20%. Samples were given an anhysteretic remanent magnetization, and were subjected subsequently to incremental compaction. The magnetic fabric shows an initially weak compaction in the printing plane that becomes larger with increased compaction. The palaeomagnetic inclination changes according to the strain that the sample undergoes, and the amount of deflection is less than predicted by a passive line model of deformation. Our results demonstrate that using a single correction factor for inclination flattening is questionable, and show the need for a method that considers how the rock deforms. Further we demonstrate the usefulness of 3D printed analogue rock, which can inspire more realistic methods to correct for inclination flattening.

1. Introduction

Palaeomagnetic directions provide essential information on the location of plates and terranes in the geological past. Inclination defines the palaeolatitude of a rock or sediment. Therefore, if bedding compaction leads to a deflection of the primary magnetization in sediments, it will have strong repercussions in palaeogeographic reconstructions. The importance of inclination flattening in sediments has been debated since the seminal work of King (1955) and numerous later studies have considered this problem (Anson and Kodama, 1987, Bilardello and Kodama, 2010, Chauvin et al., 1996, Jackson et al., 1991, Kim and Kodama, 2004, Kodama and Cox, 1978, Kodama, 1997, Lowrie et al., 1986, Tan et al., 2002). King proposed that the inclination can be corrected through the following relationship

$$tanI_R = ftanI_F \ ,$$

where I_R is the measured inclination, I_F is the expected inclination for a given latitude, and f is the flattening factor. Different f values have been applied in studies in the past and have ranged between 0.4 to just under 1.0 (Bilardello and Kodama, 2010, Bilardello, 2016). More recently studies that define global apparent polar wander curves have applied a uniform statistically based correction to all sedimentary directions. After trying different corrections factors a value was chosen that gave the best agreement between volcanic and sedimentary records (Domeier et al., 2012, Torsvik et al., 2012). The problem with this approach is that it ignores the diversity of factors that can affect the amount of flattening or deviation of the palaeomagnetic vector. Early studies demonstrated that inclination flattening depends on a number of factors, including grain size and shape (Griffiths et al., 1960), water content (Verosub et al., 1979), salinity environments and flocculation size (Tauxe et al., 2006), or small strains due to volume loss (Jackson et al., 1993). Strain and the type of deformation mechanism should have one of the strongest influences on the

amount of deviation that a palaeomagnetic vector undergoes. Any investigation on how the palaeomagnetic vector is deflected during compaction needs to be described in the framework of a deformation model. The same holds for any subsequent deformation, such as tectonic compaction.

How magnetic minerals behave in a deforming rock was addressed theoretically by Owens (1974). He proposed three models that describe how magnetic minerals react to deforming forces. These are: (i) passive model, (ii) line/plane model, and (iii) viscous model. A fourth ductile model, was later introduced by Hrouda and Lanza (1989). These models assume that magnetic grains can be approximated by ellipsoids and the grains are far enough apart to be considered magnetically non-interacting. The passive and ductile models assume that the magnetic particles change shape with deformation. Because iron oxides and iron sulphides are more rigid rheologically with respect to matrix minerals in the rock, these models are less likely to be applicable in nature. Therefore, only the passive line/plane model, in which magnetic grains react to strain as described by March (1932), and the viscous model (Jeffrey, 1922) in which the particles are considered to behave as rigid markers in a passive matrix, are considered. A short description of the deformation models that are used in this study is provided in the supplementary information.

Borradaile (1993) examined how remanence is deflected under compaction in a set of natural limestones and synthetic calcite-magnetite and calcite–hematite aggregates. He showed that the palaeomagnetic vector does not rotate as rapidly as predicted by a passive line model, therefore corrections that assume this model will overcorrect the inclination. Jackson et al. (1991) introduced a method that based the correction of inclination on the magnetic anisotropy arising from the remanence-carrying mineral phase. For ferrimagnetic carriers, preferential alignment can be estimated from the anisotropy of anhysteretic remanent magnetization (AARM). The method was further developed by the group of

Kodama (Tan and Kodama, 2003) and also extended to the anisotropy of isothermal remanent magnetization (AIRM), which would allow for correction of a hematite-bearing rock. Although this approach does not assume a deformation mechanism that is responsible for the deflection of the palaeomagnetic vector, it takes into account the amount of deformation that samples have undergone.

3-D printing is leading to new methods of conducting research in engineering, materials and life sciences (Silver, 2019). In this study we take advantage of this new approach to gain insight into the problems of how ferromagnetic minerals respond to deformation, by using 3-D printing to form rock analogues. The first use of printed rocks in geological research has focused on how the flow of liquids through rocks was influenced by porosity and permeability (Kong et al., 2018, Kong et al., 2019). We use the technique to create a set of analogue rocks that contain ferrimagnetic minerals and have porosities between 0% and 20%. The samples are given an anhysteretic remanent magnetization and then incrementally compressed to monitor the change in the magnetic fabric and palaeomagnetic vector during compression. The analogue rocks have the advantage that they can be deformed by using a simple pressure vessel, thereby avoiding problems associated with using unconsolidated sediments or large deformation rigs that can remagnetise rocks. Our results are compared with models of rock deformation, because this will dictate how any correction for inclination deflection should be made.

2. Methods

2.1. 3D-Printed Analogue Rocks

Five sets of cylinders, 1 cm in diameter and 1 cm height, were printed with porosities between 0% and 20% (Fig. 1a). Samples were assigned a Cartesian geometry in which the

X- and Y-axes lie in the printed plane, which is representative of the bedding plane in a sediment, and the Z-axis is normal to this plane, which would be representative of the pole to the bedding plane. The magnetic particles used in the analogue rocks are a commercial iron oxide (Alfa Aesar NanoArc®), which has a composition between magnetite (Fe_3O_4) and maghemite γ-Fe_2O_3) and an average particle size of 32 nm core. The spherical particles are silicon-coated. The magnetic ink was made by mixing 0.15 g of the iron oxide particles into 100 ml printing resin (Colorado Photopolymer Solutions SM412). The mixture was first stirred by hand for 5 minutes and then put in an ultrasonic bath for 15 minutes before printing the samples with an Autodesk Ember printer.

Five cylinders were printed for each porosity, corresponding to 0%, 5%, 10 %, 15% and 20 % porosity, thus giving 5 sets of 5 samples. The porosity consisted of tubes with 0.5 mm diameter and varying length that extended along the printing planes of the cylinder. Additionally, four cylindrical samples were printed of the polymer resin without magnetic nanoparticles; these samples have no porosity.

For magnetic anisotropy experiments, the samples were compressed in a cylindrical holder, which allowed for fixed increments of shortening (Supplementary Fig. 4a). The cylindrical holder was printed in an Objet 3-D printer using VeroClear^{TM} resin, which is rheologically stronger than the analogue rocks samples (Young's modulus 2-3 GPa). For the remanent magnetization experiments, samples were compressed in a pressure vessel that is a cubic holder with a 2.3 cm outer edge and a 1.4 cm inner, forming a hollow space into which the sample is inserted; one side of the cube is open to insert the sample. A flat plate that fits over the sample can be screwed down to compact the sample homogenously along the sample Z-axis (Supplementary Fig. 4b). The pressure vessel was printed with a 3-D printer using a resin, Vero^{TM} Rigid Opaque.

2.2. CT Scanning and SEM Images

The CT scans were taken with a Scanco Medical μCT50 with a power of 45kVp. 2D scans were taken by shifting the focus along the sample Z axis. Due to the different scattering between the iron-oxide particles and the resin compound with the X-rays used by the CT, different energies are capture from the X-ray detector. Based on the energy captured different pixel intensity values are set creating the 2D scans, which are post-processed using 3D Slicer and imported to Siemens NX10 for rendering the model used to extrapolate the 3D model. The Scanco Medical μCT50 has a theoretical spatial resolution of 0.5 μm on the XY plane but the practical resolution for feature reconstruction is 2 μm as stated by the manufacture. A field emission-scanning electron microscope (FE-SEM, FEI Quanta™ 450 FEG), coupled with an energy-dispersive X-ray spectrometer (EDS), was used to study the morphology and composition of minerals in the State Key Laboratory of Geological Processes and Mineral Resources of China University of Geosciences (Wuhan).

2.3. Deformation Experiments

Mechanical properties were investigated under uniaxial deformation with a Zwick/Roell universal testing machine with a 20 kN load cell. The displacement at the end-plates compressing the samples in the Z-axis was obtained by means of a built-in encoder with a resolution of 0.1 μm. The finite stiffness of the fixtures and machine frame were accounted for with a correction curve determined for the specific setup. The samples were preloaded with 5 N. All the tests were performed with a constant velocity of 2mm/min.

True stress, σ, is defined as the applied load normalized by the area of the specimen's cross-section. If l_o is the original height of the cylinder, and l is the length after applying an increment of compression, the true strain, ε, is defined as $-\ln(l/l_0)$, in which dl is the corresponding decrease in length during compaction (Chakrabarty, 2010).

2.4. Magnetic Anisotropy

Magnetic susceptibility is described mathematically by a second-order, symmetric tensor. Its eigenvalues can be represented geometrically as an ellipsoid with principal axes $k1 \geq k2 \geq k3$. Low-field anisotropy of magnetic susceptibility (LF-AMS) in SI was measured using an AGICO MFK-1 FA susceptibility bridge with an applied AC field of 200 A/m and a frequency of 976 Hz. The cylindrical holder that was used to compress the analogue rocks, fits into the holder of the susceptibility bridge used to measure the magnetic anisotropy of cubic samples, using a manual fifteen position measurement scheme. The tensor solution of the measurements was made with AGICO Anisoft (v. 4.2) software. The degree of anisotropy is defined by P' and the shape of the ellipsoid by U (Jelinek, 1981).

$$P' = exp\sqrt{2[(lnk1 - lnk)^2 + (lnk2 - lnk)^2 + (lnk3 - lnk)^2]}$$

where

$$lnk = (\ln k1 + lnk2 + lnk3)/3,$$

and

$$U = (2k2 - k1 - k3)/(k1 - k3).$$

2.5. Magnetic Remanence

All measurements of magnetic remanence were made on a 2G, 3-axis, DC SQUID, long-core cryogenic magnetometer that is outfitted with 3-coil alternating field (AF) demagnetizer and a DC coil that is aligned with the Z-axis of the AF coil. The analogue rocks were given initially an anhysteretic remanent magnetization, using a 0.1 mT DC bias-field applied on a 120 mT peak DC field, along the sample X-axis but 45° and oriented to the Z-axis. The initial remanence was measured with the sample in the pressure vessel.

The samples were then compacted incrementally and the remanent magnetisation was measured after each compaction step. Note that the pressure vessel itself did not carry a remanent magnetization.

3.   Results

3.1.   Particle Distribution

A computer-tomographic scan at nanometre scale (nano-CT) scan was made on a prototype cube to determine how the particles are distributed within the printed material. Particles are well distributed throughout the material and show a preferential alignment in the plane of flattening (XY plane; Fig. 1). It appears that the particles aggregate, even though they are coated with Si to prevent dipole-dipole interaction. It should be noted, however, that the resolution of the nano-CT scan is 200 nm; therefore, it is not possible to ascertain how closely the particles cluster.

A scanning electron microscope (SEM) image from a sample with no porosity shows some larger particles on a homogeneous background of the resin material (Supplementary Fig. 1a). The associated energy dispersive x-ray spectrum (SEM-EDS) indicates that iron distributes evenly in the resin of the samples, which is consistent with the CT scans (Supplementary Fig. 1b). Based on the distribution of elements, it can be concluded that the resin consists mainly of oxygen and carbon (Supplementary Fig. 1c, d) with minor proportions of sodium, potassium and chlorine and trace amounts of sulphur (Supplementary Fig. 1e-h). The large particles are composed of Na, Cl and K, indicative of the formation of halite.
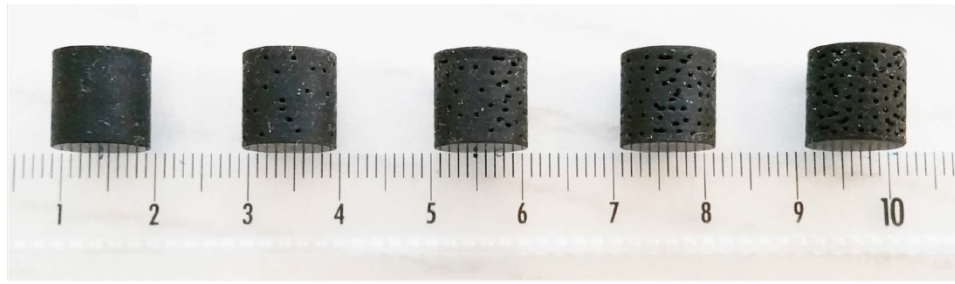
a)

b)
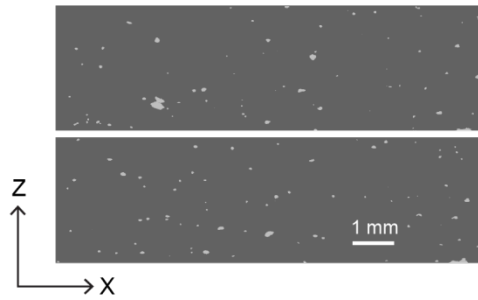
c)

Fig. 1: Sample description. a) 3-D printed samples with no porosity and 5%, 10%, 15% and 20% porosity. b) Schematic illustration of a printed cylinder with 5% pore space. c) Two examples of CT scans for 2-D sections in the X-Z plane for a sample that has not undergone any compaction. It illustrates the preferential alignment of particles in the printing (X-Y) plane.

3.2. Elastic Properties

The axial deformation results show a typical evolution of the non-linear viscoelastic stress-response typical for rubber. The sample undergoes large reversible deformation at relatively small applied axial stress (Fig. 2). This typical viscoelastic behaviour of the resin is due to the elastic responses of the molecular chains crosslinked in the network sample. For low porosity, the difference in the stress-strain curve is within the accuracy of the system. Only the sample with higher porosity (ca. 20%) shows a weaker, but similar, trend.
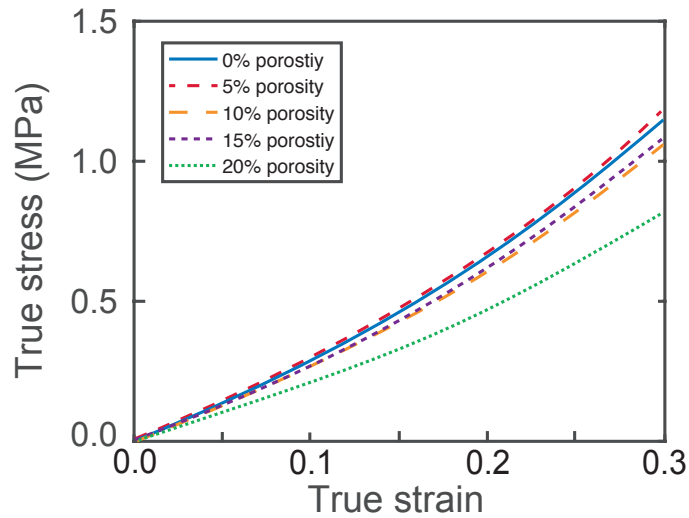
Fig. 2: Stress-strain relationships for analogue rocks. True stress as a function of true strain for one sample of each porosity illustrating non-linear elastic deformation.

3.3. Rock Magnetic Properties

The magnetic nanoparticles used in the printing ink, were purchased from ASEA (NanoArc®), and their magnetic properties were characterized first in powder form. The composition is given as maghaemite (γ-Fe_2O_3) with an average particle size of 32 nm. Magnetic hysteresis shows an open loop that is close to saturation by 300 mT. Saturation magnetization (M_S) is 79.0 Am^2kg^{-1} and magnetic coercivity (B_C) is 15.5 mT (Supplementary Fig. 2a), which is compatible with single domain maghaemite or cation-deficient magnetite. Back-field isothermal remanent magnetization (IRM) shows a coercivity of remanence (B_{CR}) of 26.8 mT (Supplementary Fig. 2b). Analysis of first-order reversal curves (FORC), which provides information about the coercivity spectrum of the maghaemite powder (Supplementary. Fig. 2c), shows a bimodal coercivity distribution with a very low coercivity contribution (< 2 mT) and a distributed coercivity between 4 and 80 mT with a peak coercivity of 23 mT (Supplementary Fig. 2e).

The magnetic properties of the analogue rock were measured to assess if the ferromagnetic nanoparticles had undergone any alteration during the printing process. Note that the magnetization was normalized to the amount of maghaemite in the sample, by assuming a concentration of 0.15%. Magnetic hysteresis and backfield IRM acquisition curves are similar to the original powder, although B_{CR} is marginally higher at 29.6 mT (Supplementary Fig. 2a, b). The FORC diagram is also similar to the original powder with a bimodal coercivity distribution (Supplementary Fig. 2d); however, both the lower and higher peak coercivities are broader and higher than for the original powder (Supplementary Fig. 2e). This may be due to some surface oxidation of the original particles during printing.

3.4. Magnetic Anisotropy

The low-field AMS of samples that contain no magnetic nanoparticles are diamagnetic and statistically isotropic, even under compaction. Therefore, the printing resin of the analogue rocks does not affect their magnetic anisotropy and its contribution can be ignored. The magnetic susceptibility of all undeformed cylindrical samples is $8.858 \pm 0.295 \times 10^{-4}$ SI. The small variation between samples attests to the homogenous distribution of magnetic nanoparticles in the print resin. The initial low-field AMS shows a weak oblate fabric with 4.7 ± 0.6 % flattening in the printing plane (Fig. 3a), and the shape of the AMS ellipsoid varies between U = 0.178 to 0.771 (Fig. 3b). The k3-axes of all samples are within 10° from the normal to the printing plane, except for one cylinder with 15% porosity, in which has k3 oriented 20° from the normal (Supplementary Fig. 3, Supplementary Table 1).

Samples were subjected to four steps of incremental compaction resulting in 5%, 10 %, 15 % and 22.5% shortening using a pressure vessel that is shown in Supplementary Fig. 4a. It was not possible to compress the samples further with the pressure vessel that was used

for the AMS measurements. Bulk susceptibility increases with each compaction step (Supplementary Table 1). The degree of anisotropy, P_j, increases linearly in general, although there is a smaller change for 15% compaction (Fig. 3a) for all samples regardless of the sample porosity (Supplementary Fig. 5a). The shape of the AMS ellipsoid becomes more oblate with compaction (Fig. 3b). The variation in U for any given compaction-step, however decreases with increasing compaction (Supplementary Fig. 5b), and – similar to P_j – U is not affected systematically by the porosity of the sample. With regards to directional data, the k3 axes of the AMS ellipsoid move closer to the compaction pole and are within 4° from the pole for the majority of samples (Supplementary Fig. 3, Supplementary Table 1).
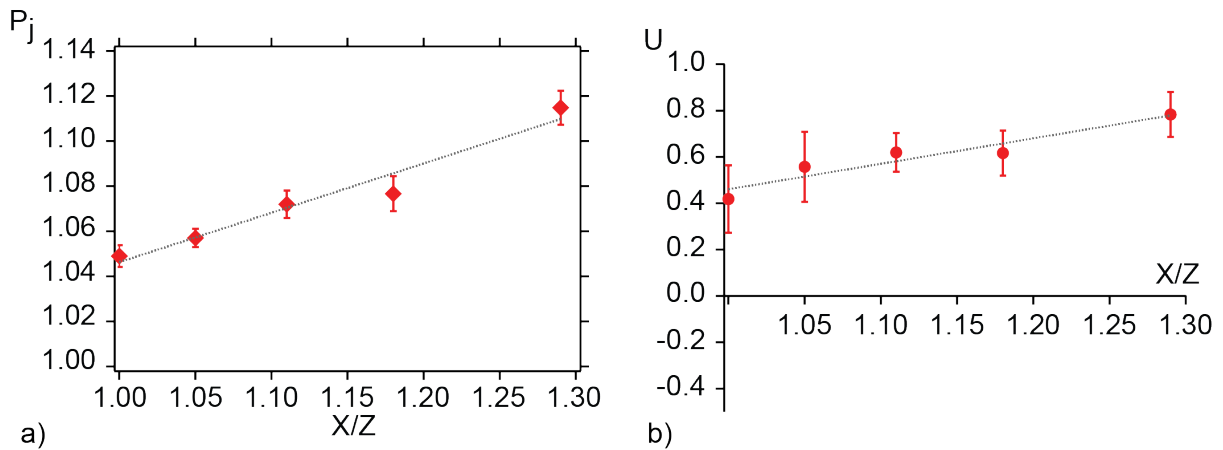
Fig. 3: Ferromagnetic anisotropy as a function of compaction. a) Change in the average degree of anisotropy, and b) the average shape of the AMS ellipsoid with increasing compaction. Error bars show one standard deviation.

3.5. Magnetic Remanence and Deformation Behaviour

Samples that do not contain magnetic nanoparticles have no initial remanent magnetization and do not acquire an ARM, as would be expected if there is no ferromagnetic component in the sample. The initial intensity of the anhysteretic remanent magnetisation (ARM) of samples with magnetic nanoparticles is more variable than the

bulk susceptibility, and is between 2.29 x 10^{-4} and 4.71 x 10^{-3} A/m with an average value of

3.15 ± 0.74 x 10^{-4} A/m (Supplementary Table 2). Although the field used to apply the ARM

should give an inclination of 45° with respect to the Z-axis, the inclination varies between

20.6° and 58.8°. The difference between the imparted inclination and the applied field is

not related statistically with a sample's porosity or degree of anisotropy, and at present we

do not understand the cause of this discrepancy; this point is discussed further below.
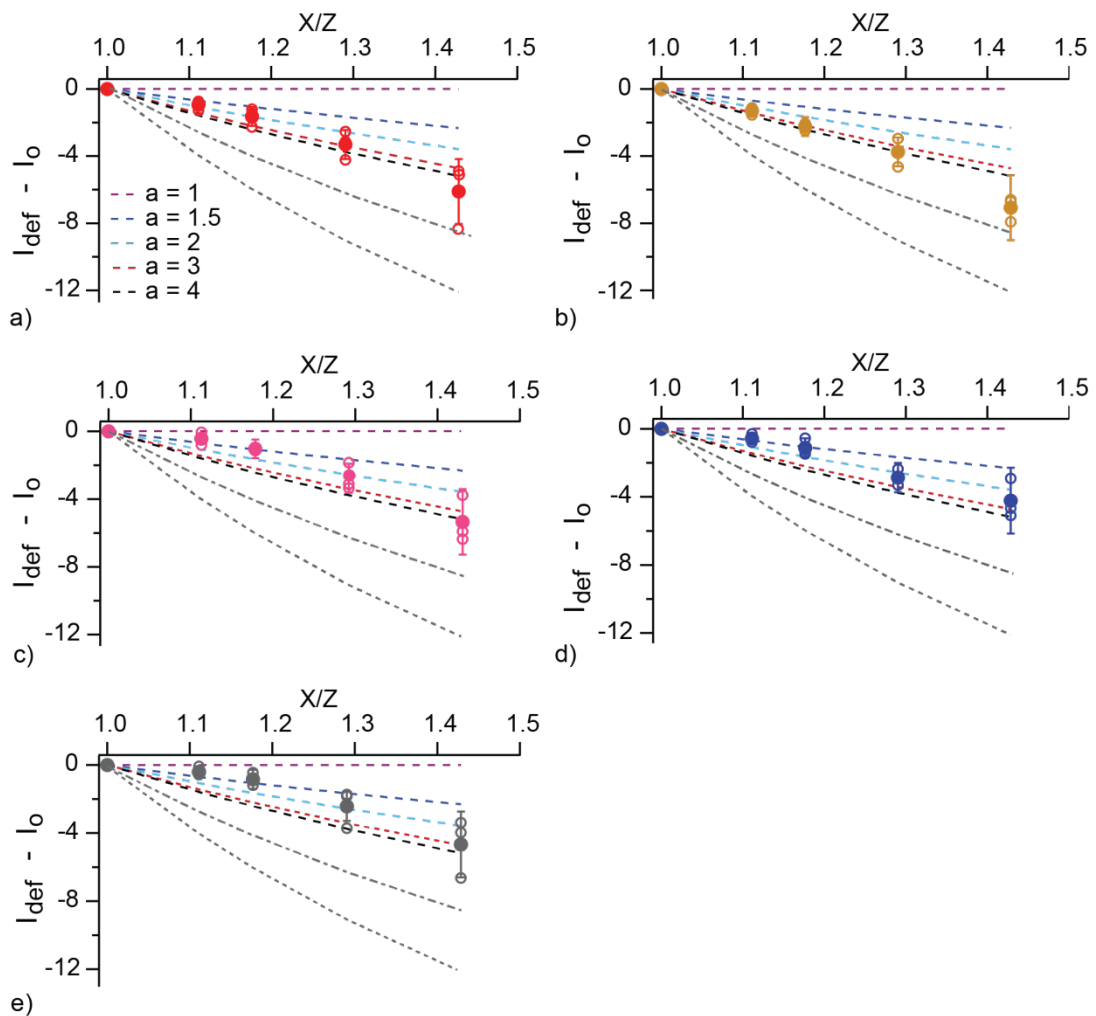
Fig. 4. Mean deviation (filled circle) of the original inclination for the four samples (open

circles) of the same porosity as a function of compaction and porosity. Samples with a) no

porosity, b) 5% porosity, c) 10% porosity, d) 15% porosity, and e) 20% porosity. Dashed

grey line shows the expected deviation from the mean for a passive line model in 3-D and

the dashed-dotted grey line for 2-D, and coloured dashed lines (reader is referred to web

version of this article) illustrate the predicted deviation for rigid particles with different aspect ratios in a viscous matrix.

Four samples from each of the five sets of cylinders were incrementally compacted and the ARM was measured after each compaction step. Inclination becomes shallower with each compaction step for all samples, and the amount of deflection increases with increasing compaction (Supplementary Table 2). Fig. 4 shows the mean deviation in inclination for each of the four sets as a function of compaction. The amount of deviation of all samples is not as large as that predicted by a March model in either 2-D or 3-D. This indicates that the magnetic nanoparticles – and hence the ARM vector – do not behave like a passive line during compaction. The small degree of deflection suggests that the magnetic nanoparticles respond more like a rigid marker in a viscous matrix. In this case, the amount of deflection will be dependent on the aspect ratio (i.e., ratio of the long axis to short axis) of the nanoparticles. If the particles are equi-dimensional, the grains would not be expected to rotate and remanence would not deflect. We compare the amount of deflection of inclination for rigid markers that have an aspect ratio from 1:1 to 4:1. For compaction up to 15%, the inclination behaves as a rigid marker for particles with an aspect ratio between 1.5 and 2, except for the samples with 5% porosity. At higher degrees of compaction, however, the samples show a larger amount of deviation, which suggest that the purely rigid marker method in a viscous matrix is not applicable. What we note, however, is that the deflection of inclination follows the stress-strain relationship (Fig. 5). The amount of deflection is related to porosity, with low-to-no porosity showing larger deflection than higher porosity. This suggests that while pore space is being closed, the matrix undergoes little deformation such that inclination is not affected significantly.

4. Discussion

We have demonstrated that it is possible to distribute a weak concentration of coated ferromagnetic particles throughout a resin to print samples that serve as analogue rocks. Although some clustering of particles occurs as seen in CT scans (Fig. 1), the resolution of the scans is not high enough resolution to establish the distance between particles in the clusters. The magnetic properties of the printed material, however, do not change significantly, which suggests that magnetic interactions are minimal.
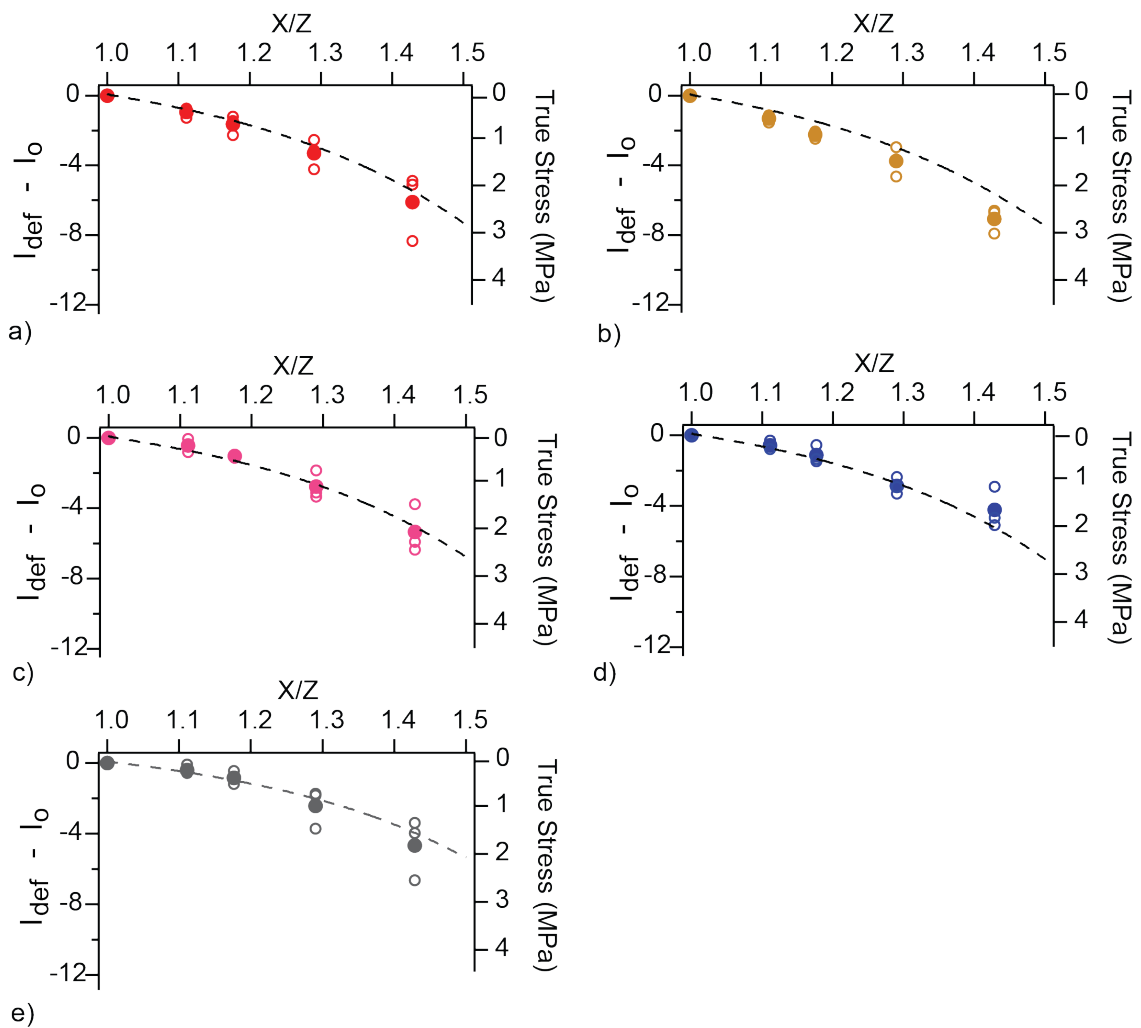

Fig. 5: Deflection of inclination from its original inclination compared to the stress-strain relationship. Average change in original inclination (filled circle) for four samples of the same porosity (open circles) as a function of compaction, porosity compared with relationship of true stress as a function of true strain. Samples with a) no porosity, b) 5%

porosity, c) 10% porosity, d) 15% porosity, and e) 20% porosity. Black dashed line show the relationship of extension to true stress (black dashed line).

The relationship of true stress to true strain demonstrate that the samples show nonlinear elastic behaviour under compression. At high strain, the samples do not return completely to their original shape, which indicates that some plastic deformation may have occurred. Although many natural rocks that undergo deformation show linear elastic behaviour for low strain and then plastic deformation at higher strain, it is not uncommon that natural rocks display non-linear elastic behaviour (Nejati et al., 2019). For example, the non-linear viscoelastic relationship between stress and strain is similar to what one observed in an initial loading and unloading path performed in a uniaxial test when the microcracks are closed during loading (Minardi et al., 2018). Further parallels to deformed re-sedimented sediments and to rocks deformed in deformation rigs are discussed below.

Samples without any ferromagnetic particles do not have a significant magnetic anisotropy in their initial state or with increasing deformation under compaction. Therefore any magnetic fabric arises solely from the alignment of the ferromagnetic particles in the printing resin. The samples with ferromagnetic particles have an oblate magnetic fabric with flattening in the plane of printing. The degree of flattening is between 3 and 6 %, which is typical for what is found in undeformed sediments (Fig. 3, Supplementary Fig. 5) (Cifelli et al., 2004, Graham, 1966, Hirt et al., 1995, Parés et al., 1999). As the samples undergo compaction the degree of anisotropy and degree of flattening increase, as shown by the monotonic increase in both P' and to a lesser extent U. This indicates that the particles are becoming more aligned statistically in the plane of compression. It is this realignment that will affect the magnetic inclination.

Although the magnetic fabrics of all printed samples are initially similar, we observe

differences in the direction of the acquired ARM that was applied at an angle of 45 ° from the cylinder Z-axis. The samples that do not contain ferromagnetic particles do not acquire an ARM, indicating that the resin material does not contribute to the remanence. Because the initial degree of anisotropy is low, there cannot be a strong alignment in the printing plane. In addition, there is no clear relationship with porosity or printing series and the initial inclination, therefore it does not appear as if the ferromagnetic minerals are collecting on pore surfaces. At present, we do not understand why this variation occurs, but future experiments will investigate if printing process leads to a preference in direction, which is associated with printing speed. The range of initial inclinations, however is fortuitous, because we demonstrate that regardless of the initial inclination, samples with the same porosity all show that the mean deviation of inclination follows the strain relationship (Fig. 5). Whether the inclination of a sample is either slightly above or below the mean inclination during compaction, is not related to its initial inclination.

The change in magnetic inclination is directly related to the strain in which the sample has undergone, as has been noted by Borradaile (1993). The amount of deflection follows the increase in strain for higher deformation (Fig. 5). Correction for inclination flattening, which is not based on measuring the anisotropy of remanence of samples, has often assumed that magnetic inclination behaves as a passive line or plane. As seen from the deformation experiments this model in 3D predicts a much larger amount of deflection, compared to what actually occurs. A simpler 2D behaviour as suggested by Ramsay (1967) also over-predicts the amount of deformation. As Borradaile (1993) stated, a rigid marker in a viscous matrix is mechanically the most realistic model. In our study the inclination deviations agree with a rigid particle model at low strains but they do not follow a rigid marker model at higher degrees of deformation, where they are more closely related to strain-behaviour. This leads to the question if the analogue rocks are a suitable model for

natural rocks. In the following we compare our results to earlier studies that have examined the deflection of inclination due to compaction or deformation.

Tan et al. (2002) examined inclination deviation due to compaction by redepositing disaggregated redbeds of Eocene age in a known magnetic field. After re-sedimentation, the samples were compacted. The compaction only started once friction between filter paper on top of the sediment and the plunger were overcome. Although hematite was the ferromagnetic mineral that carried the magnetization in Tan et al. (2002), there is a slow deflection of inclination for low strain or volume loss and an increase at higher deformation, similar to what is observed in our analogue rocks. Borradaile (1993) also noted in a set of limestone, sandstone, and magnetite-calcite aggregates, that inclination showed little deflection at low strain, and an increasing deflection with higher strain. He demonstrated that correction for inclination using a passive line model led to a small overcorrection in most cases.

These studies indicate that we are in need of a better understanding of how the direction of magnetic remanence, in particular inclination, can be deflected by either bedding or tectonic deflected compaction. Most studies assume that deformation consists of pure strain without change in volume. We show that in our samples that have a porosity the amount of inclination deflection is low until the pore space is closed, and this is probably true in other experimental studies that assume that rocks deform passively. Although this approach does not take into account diagenetic processes that can lead to formation of ferromagnetic minerals during or at a late stage of compaction, our experiments demonstrate that 3D printed analogue rocks can provide insight into the relationship between deformation and magnetic remanence. With advancement in 3D printing technology, a wider range of materials with different rheologies is becoming available. In the future it will be possible to mix geologic materials, such as sand or clay particles, in

addition to ferromagnetic grains together with the resins to mimic more natural rock-like deformation (Kong et al., 2018, Kong et al., 2019). Future experiments should also focus on hematite as the main ferromagnetic minerals or on ferromagnetic minerals with different particle size distributions to investigate the role of particle size. The main limitation in different materials is the ability to be able to compact these without altering the original magnetization through remagnetization.

In conclusion, our results show that passive marker corrections have a tendency to overcorrect the magnetic inclination, which in terms of paleomagnetism would suggest the rock acquired its magnetization at a higher latitude than it really did. Methods that use a scaling factor based on the anisotropy of ARM to correct remanent magnetization may give a more reliable estimate of inclination deflection (Li and Kodama, 2016), because the rheology of the rock is indirectly taken into account.

Acknowledgements

References

Anson, G. L., Kodama, K. P., 1987. Compaction-induced inclination shallowing of the post-depositional remanent magnetization in a synthetic sediment. Geophysical Journal International 88, 673-692. https://doi.org/10.1111/j.1365-246X.1987. tb01651.x.

Bilardello, D., Kodama, K. P., 2010. A new inclination shallowing correction of the Mauch Chunk Formation of Pennsylvania, based on high-field AIR results: Implications for the Carboniferous North American APW path and Pangea reconstructions. Earth and Planetary Science Letters 299, 218-227. https://doi.org/10.1016/j.epsl.2010.09.002.

Bilardello, D., 2016. The do's and don't's of inclination shallowing corrections. The IRM Quarterly 26 (3).

Borradaile, G. J., 1993. Strain and magnetic remanence. Journal of Structural Geology 15, 383-390. https://doi.org/10.1016/0191-8141(93)90134-V.

Chakrabarty, J.,   2010.Applied Plasticity. Springer.

Chauvin, A., Perroud, H., Bazhenov, M. L., 1996. Anomalous low palaeomagnetic inclinations from Oligocene—Lower Miocene red beds of the south-west Tien

Shan, Central Asia. Geophysical Journal International 126, 303-313. https://doi.org/ 10.1111/j.1365-246X.1996.tb05293.x.

Cifelli, F., Rossetti, F., Mattei, M., Hirt, A. M., Funiciello, R., Tortorici, L., 2004. An AMS, structural and paleomagnetic study of quaternary deformation in eastern Sicily. Journal of Structural Geology 26, 29-46. https://doi.org/10.1016/S0191-8141 (03)00092-0.

Domeier, M., Voo, R. V. D., Torsvik, T. H., 2012. Paleomagnetism and Pangea: The road to reconciliation. Tectonophysics 514–517, 14-43. https://doi.org/10.1016/j.tecto. 2011.10.021.

Graham, J. W. Significance of magnetic anisotropy in Appalachian sedimentary rocks. In: Steinhart J. S.,Smith T. J. (eds). The Earth Beneath the Continents, Geophysical Monograph 10. American Geophysical Union: Washington, 1966, pp 627-648.

Griffiths, D. H., King, R. F., Rees, A. I., Wright, A. E., 1960. The remanent magnetism of some recent varved sediments. Proceedings of the Royal Society of London 256, 359-383. https://doi.org/10.1098/rspb.1960.0092.

Hirt, A. M., Evans, K. F., Engelder, T., 1995. Correlation between magnetic anisotropy and fabric for Devonian shales on the Appalachian Plateau. Tectonophysics 247, 121-132. https://doi.org/10.1016/0040-1951(94)00176-A.

Hrouda, F., Lanza, R., 1989. Magnetic fabric in the Biella and Traversella stocks (Periadriatic Line): implications for the mode of emplacement. Physics of the Earth and Planetary Interiors 56, 337-348. https://doi.org/10.1016/0031-9201(89)90168-4.

Jackson, M., Borradaile, G., Hudleston, P., Banerjee, S., 1993. Experimental deformation of synthetic magnetite-bearing calcite sandstones: Effects on remanence, bulk magnetic properties, and magnetic anisotropy. Journal of Geophysical Research: Solid Earth 98, 383-401. https://doi.org/10.1029/92JB01028.

Jackson, M. J., Banerjee, S. K., Marvin, J. A., Lu, R., Gruber, W., 1991. Detrital remanence, inclination errors, and anhysteretic remanence anisotropy: quantitative model and experimental results. Geophysical Journal International 104, 95-103. https://doi.org/ 10.1111/j.1365-246X.1991.tb02496.x.

Jeffrey, G. B., 1922. The motion of ellipsoidal particles immersed in a viscous fluid. Proc R Soc London 102, 161-179.

Jelinek, V., 1981. Characterization of the magnetic fabric of rocks. Tectonophysics 79, T63-T67. https://doi.org/10.1016/0040-1951(81)90110-4.

Kim, B., Kodama, K. P., 2004. A compaction correction for the paleomagnetism of the Nanaimo Group sedimentary rocks: Implications for the Baja British Columbia hypothesis. Journal of Geophysical Research: Solid Earth 109, B02102. https: //doi.org/10.1029/2003JB002696.

King, R. F., 1955. The remanent magnetism of artificially deposited sediments. Geophysical Supplements to the Monthly Notices of the Royal Astronomical Society 7, 115-134. https://doi.org/10.1111/j.1365-246X.1955.tb06558.x.

Kodama, K. P., Cox, A., 1978. The effects of a constant volume deformation on the magnetization of an artificial sediment. Earth and Planetary Science Letters 38, 436-442. https://doi.org/10.1016/0012-821X(78)90118-8.

Kodama, K. P., 1997. A successful rock magnetic technique for correctng paleomagnetic inclination shallowing: Case study of the Nacimiento Formation, New Mexico. Journal of Geophysical Research: Solid Earth 102, 5193-5205. https://doi.org /10.1029/96JB03833.

Kong, L., Ostadhassan, M., Li, C., Tamimi, N., 2018. Can 3-D printed gypsum samples replicate natural rocks? An experimental study. Rock Mechanics and Rock Engineering 51, 3061-3074. https://doi.org/10.1007/s00603-018-1520-3.

Kong, L., Ostadhassan, M., Hou, X., Mann, M., Li, C., 2019. Microstructure characteristics and fractal analysis of 3D-printed sandstone using micro-CT and SEM-EDS. Journal of Petroleum Science and Engineering 175, 1039-1048. https://doi.org/10.1016 /j.petrol.2019.01.050.

Li, Y., Kodama, K. P., 2016. Detecting and correcting for paleomagnetic inclination shallowing of sedimentary rocks: A review. Frontiers in Earth Science 4, doi:10.3389/feart.2016.00007. https://doi.org/10.3389/feart.2016.00007.

Lowrie, W., Hirt, A. M., Kligfield, R., 1986. Effects of tectonic deformation on the remanent magnetization of rocks. Tectonics 5, 713–722. https://doi.org/10.1029 /TC005i005p00713.

March, A., 1932. Mathematische Theorie der Regelung nach der Korngestalt bei affiner Deformation. Z Kristallogr 81, 285-297.

Minardi, A., Ferrari, A., Ewy, R., Laloui, L., 2018. Nonlinear Elastic Response of Partially Saturated Gas Shales in Uniaxial Compression. Rock Mechanics and Rock Engineering 51, 1967-1978. https://doi.org/10.1007/s00603-018-1453-x.

Nejati, M., Texas, M. L., Saar, M. O., 2019. A methodology to determine the elastic properties of anisotropic rocks from a single uniaxial compression test. Journal of Rock Mechanics and Geotechnical Engineering 11, 1166-1183.. https://doi.org/ 10.1016/ j.jrmge.2019.04.004.

Owens, W. H., 1974. Mathematical model studies on factors affecting the magnetic anisotropy of deformed rocks. Tectonophysics 24, 115-131. https://doi.org/10.1016/ 0040-1951(74)90133-4.

Parés, J. M., van der Pluijm, B. A., Dinarès-Turell, J., 1999. Evolution of magnetic fabrics during incipient deformation of mudrocks (Pyrenees, northern Spain). Tectonophysics 307, 1-14. https://doi.org/10.1016/S0040-1951(99)00115-8.

Ramsay, J. G., 1967.Folding and Fracture of Rocks. McGraw Hill: New York.

Silver, A., 2019. 3D printing in the Lab. Nature 565, 123-124.

Tan, X., Kodama, K. P., Fang, D., 2002. Laboratory depositional and compaction-caused inclination errors carried by haematite and their implications in identifying inclination error of natural remanence in red beds. Geophysical Journal International 151, 475-486. https://doi.org/10.1046/j.1365-246X.2002.01794.x.

Tan, X., Kodama, K. P., 2003. An analytical solution for correcting palaeomagnetic inclination error. Geophysical Journal International 152, 228-236. https://doi.org/ 10.1046/j.1365-246X.2003.01848.x.

Tauxe, L., Steindorf, J. L., Harris, A., 2006. Depositional remanent magnetization: Toward an improved theoretical and experimental foundation. Earth and Planetary Science Letters 244, 515-529. https://doi.org/10.1016/j.epsl.2006.02.003.

Torsvik, T. H., Van der Voo, R., Preeden, U., Mac Niocaill, C., Steinberger, B., Doubrovine, P. V., van Hinsbergen, D. J. J., Domeier, M., Gaina, C., Tohver, E., Meert, J. G., McCausland, P. J. A., Cocks, L. R. M., 2012. Phanerozoic polar wander, palaeogeography and dynamics. Earth-Science Reviews 114, 325-368. https://doi.org/ 10.1016/j.earscirev.2012.06.007.

Verosub, K. L., Ensley, R. A., Ulrick, J. S., 1979. The role of water content in the magnetization of sediments. Geophysical Research Letters 6, 226-228. https:// doi.org/10.1029/GL006i004p00226.

Additional Information

The supplementary information file contains a short description of the deformation models, five additional figures showing the detailed results, and two tables that list all measurement data that are used in this study.

Supplementary Information

Deformation Models

All deformation models assume that magnetic grains can be approximated by ellipsoids and the grains are far enough apart to be considered magnetically non-interacting.

Passive Line/Plane Model

The Line/Plane, i.e., March, model of deformation assumes that the ferromagnetic grains behave like material lines or planes, which implies that the paleomagnetic vector also deforms in this manner in a homogeneous matrix. Paleomagnetic inclination that is subjected to flattening either due to sedimentary or tectonic compaction will change as a function of strain. If inclination makes an angle α_o with respect to the plane of flattening, it will change its orientation to α in response to the strain, which is defined from the change in shape of the body. We can consider a cylinder in which Z is the parallel to the cylinder axis and the plane of the cylinder has X = Y in the basal plane. If the cylinder is subjected to flattening along Z, we can describe deformation in terms of pure shear, in which X = 1/Z and Y=1 in the two-dimensional case. The deflection of a line is described by Wettstein's equation[1] (eqn. 3.34):

$$\frac{\tan \alpha}{\tan \alpha_o} = \frac{Z}{X}.$$ Eqn. 1

For the three-dimensional case of coaxial perfect flattening, in which $X = Y > Z$ and constant volume $X \cdot Y \cdot Z = 1$, the deflection of a line or planes with respect to the Z axis has been described by Borradaile[2] (eqn. 2) as:

$$\frac{\tan \alpha}{\tan \alpha_o} = Z^{1.5}.$$ Eqn. 2

We use Eqn. 2 for predicting the change of inclination for a Passive Line/Plane model.

Rigid Marker Model

Because ferromagnetic particles are generally rigid compared to minerals in the matrix, particularly in the case of shale or lacustrine sediment, we can view this case as rigid markers deforming in a passive matrix[3]. A rigid elliptical marker with an average aspect ratio a will rotate in an incompressible elastic medium when undergoing pure shear, and the rate of rotation of the long axis can be expressed in terms of extension in the X-direction of the matrix[3] (eqn. 2). In the case of perfect flattening $X^2 = 1/Z$, Borradaile[4] (eqn. 7) shows the deflection of the long axis will be dependent on a, and the logarithmic extension ε_X, where,

$\varepsilon_X = \frac{1}{3} \ln(R)$ and $R = X/Z$.

The deflection of α_o to α, can be expressed as:

$$\frac{1}{2} \ln(\tan \alpha) - \frac{1}{2} \ln(\tan \alpha_o) = \frac{(a^2-1)}{(a^2+1)} \cdot \varepsilon_X. \qquad \text{Eqn. 3}$$

References

1   Ramsay, J. G. *Folding and Fracture of Rocks*.   (McGraw Hill, 1967).
2   Borradaile, G. J. & Henry, B. Tectonic application of magnetic susceptibility and its anisotropy. *Earth Science Review* **42**, 49-93 (1997).
3   Ghosh, S. K. & Ramberg, H. Reorientation of inclusions by combination of pure shear and simple shear. *Tectonohyscis* **34**, 1-70, doi:10.1016/0040-1951(76)90176-1 (1976).
4   Borradaile, G. Strain and magnetic remanence. *Journal of Structural Geology* **15**, 383-390, doi:10.1016/0191-8141(93)90134-v (1993).

Supplementary Figures
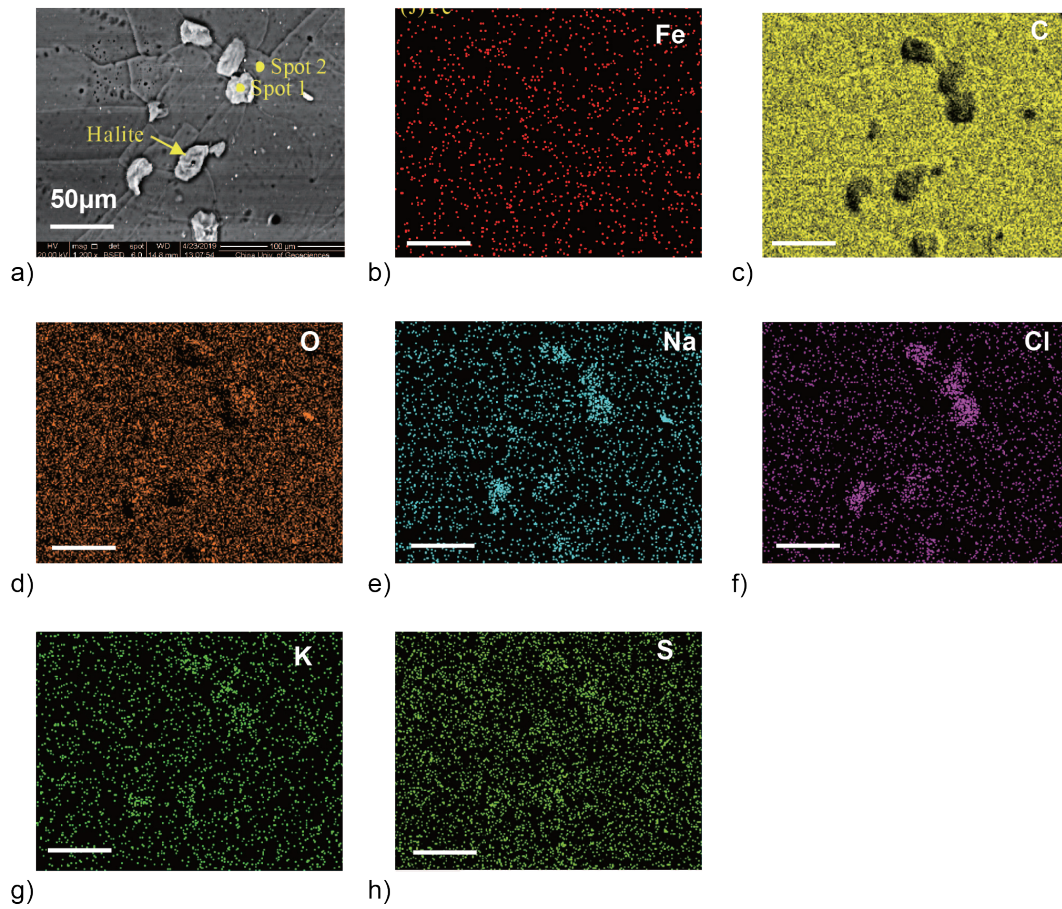
Supplementary Figure 1: SEM-EDS spectra. a) backscatter image, and elemental distribution for b) Fe. Based on the distribution of elements, it can be concluded that the resin consists mainly of c) C and d) O with minor proportions of e) Na, f) Cl, g) K, and trace amounts of h) S. The large particles are composed of Na, Cl and K, indicative of the formation of halite. Scale bar is 50 μm.
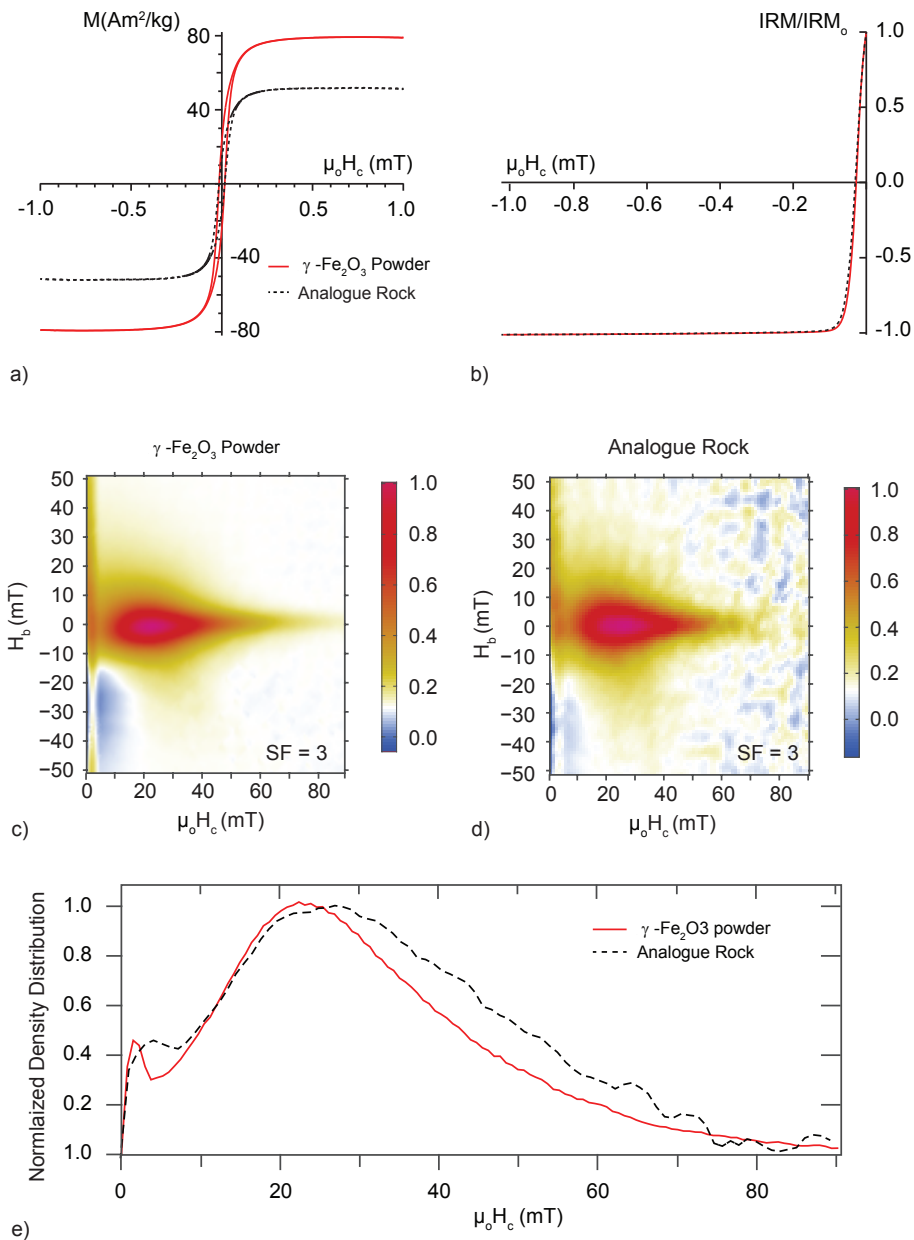
Supplementary Figure 2: Rock magnetic properties of Asea NanoArc® powder and printed analogue rock. a) Magnetic hysteresis loops, b) back-field acquisition of IRM, c, FORC diagram for the powder sample, d) FORC diagram for an analogue rock sample, and e) comparison of coercivity spectrum for the original powder and analogue rock.
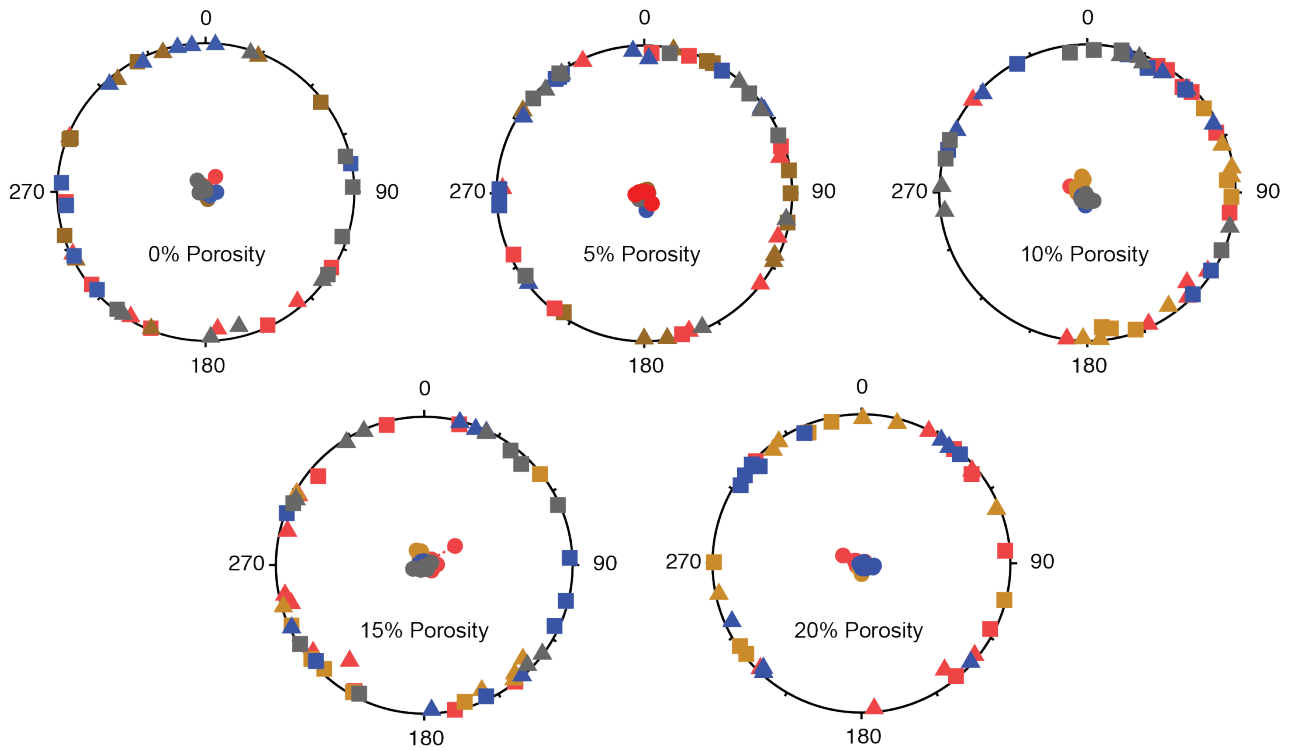
Supplementary Figure 3: Summary of AMS results. Lower hemisphere, equal area projection showing the change in orientation of the principal axes of the AMS ellipsoid for all samples as a function of their porosity. The four sets of samples are distinguished by the different color symbols; k1 is shown as squares, k2 as triangles and k3 as circles.
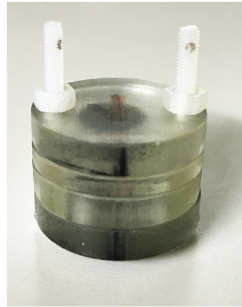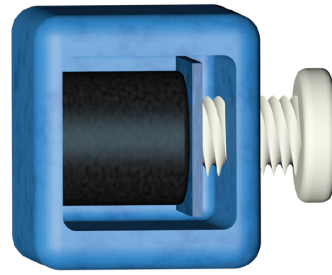
a)   b)

Supplementary Figure 4: Pressure vessels. a) Printed pressure vessel that can be screwed down to compact samples during AMS measurements, and b) schematic drawing of printed pressure vessel used to compact samples for remanent measurements.   Note that the pressure vessel limited compaction to a maximum of 22.5 % for the AMS measurements, and 30 % for the remanent measurements.
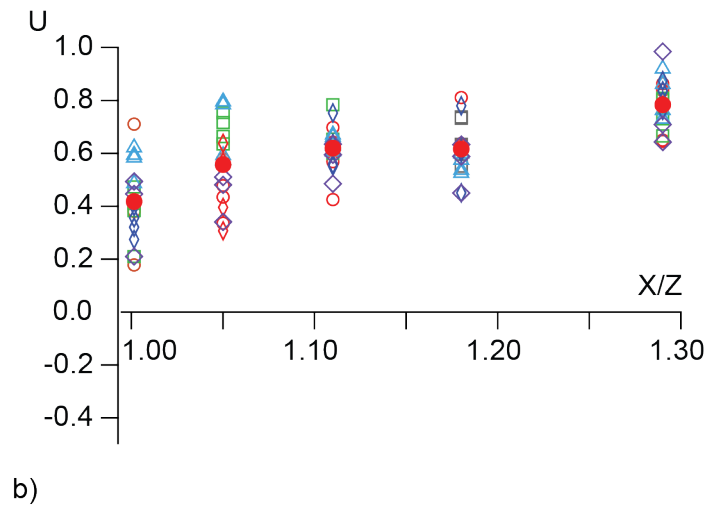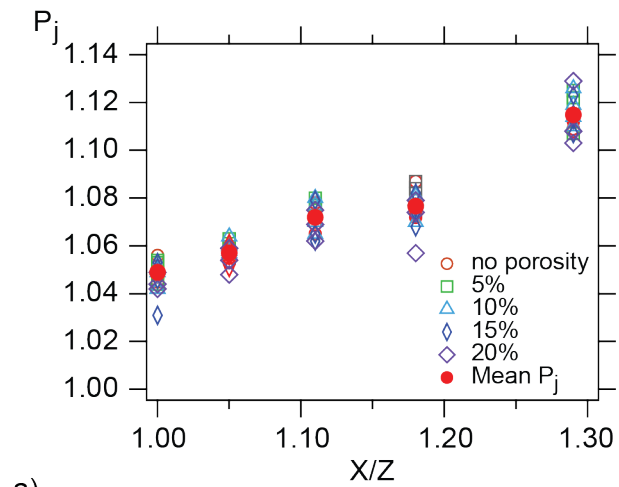
Supplementary Figure 5: Anisotropy parameter shown as a function of compaction for all samples. a) Change in P_j, and b) U for individual samples as a function of compaction with different porosity. The mean value of P_j or U is shown by the red circle for each porosity.

Supplementary Table Captions

Suppl. Table 1: Summary of low-field AMS with mean susceptibility, eigenvalues and directions of the principal susceptibility axes, and anisotropy parameters. a) Sample set A, b) sample set B, c) sample set C, and d) sample set D.

Suppl. Table 2: Summary of ARM shallowing as a function of compaction. a) Sample set A, b) sample set B, c) sample set C, and d) sample set D.

Supplementary Table 1: Summary of low-field AMS with mean susceptibility, eigenvalues and directions of the principal susceptibility axes, and anisotropy parameters. a) Sample set A.

Porosity (%)	Compaction (%)	k_{Mean}	Maximum axis			Intermediate axis			Minimum axis			U	Pj
			K_1	D1(°)	I1(°)	K_2	D2(°)	I2(°)	K_3	D3(°)	I3(°)		
0	0.0	9.092E-04	1.019	52.1	1.6	1.006	322.0	3.9	0.974	164.0	85.8	0.411	1.047
	5.0	9.260E-04	1.021	332.3	0.7	1.008	242.3	1.2	0.9711	91.1	88.6	0.478	1.053
	10.0	9.293E-04	1.026	291.1	1.4	1.016	21.2	1.8	0.957	164.8	87.7	0.698	1.078
	15.0	9.474E-04	1.027	291.8	2.2	1.020	201.8	0.8	0.952	91.4	87.7	0.811	1.087
	22.5	9.408E-04	1.037	252.9	0.3	1.020	342.9	1.6	0.942	151.2	88.4	0.645	1.108
5	0.0	9.222E-04	1.023	90.0	0.6	1.003	180.1	1.4	0.972	336.0	88.5	0.210	1.053
	5.0	9.366E-04	1.018	214.2	2.7	1.012	304.2	0.1	0.968	35.4	87.3	0.754	1.057
	10.0	9.434E-04	1.028	25.3	0.5	1.014	115.3	2.2	0.956	283.4	87.8	0.617	1.080
	15.0	9.606E-04	1.031	101.5	0.8	1.014	11.5	0.5	0.954	253.0	89.0	0.552	1.084
	22.5	9.596E-04	1.040	81.0	0.5	1.023	171.0	0.4	0.936	300.2	89.4	0.666	1.120
10	0.0	9.010E-04	1.015	173.9	9.2	1.007	83.6	2.1	0.977	340.9	80.6	0.584	1.042
	5.0	9.159E-04	1.018	170.2	7.4	1.013	80.1	0.7	0.968	344.4	82.6	0.785	1.057
	10.0	9.214E-04	1.024	84.9	5.6	1.013	175.0	0.3	0.962	268.0	84.4	0.662	1.070
	15.0	9.385E-04	1.029	91.6	2.5	1.012	181.7	1.3	0.957	298.4	87.2	0.526	1.079
	22.5	9.368E-04	1.032	160.6	1.8	1.028	70.5	3.4	0.938	279.2	86.2	0.920	1.114
15	0.0	8.797E-04	1.021	224.0	2.9	1.005	133.5	8.7	0.973	332.5	80.9	0.356	1.051
	5.0	8.934E-04	1.022	230.3	0.7	1.010	140.2	4.9	0.966	328.3	85.0	0.568	1.061
	10.0	8.985E-04	1.023	51.8	0.3	1.012	141.8	1.7	0.964	310.6	88.2	0.637	1.065
	15.0	9.157E-04	1.027	209.3	1.6	1.014	299.3	1.0	0.958	61.8	88.1	0.618	1.076
	22.5	9.153E-04	1.034	163.5	4.0	1.026	253.6	0.6	0.938	351.8	85.9	0.836	1.115

Supplementary Table 1(continued). b) Sample set B.

Porosity (%)	Compaction (%)	k_{Mean}	Maximum axis			Intermediate axis			Minimum axis			U	Pj
			K_1	D1(°)	I1(°)	K_2	D2(°)	I2(°)	K_3	D3(°)	I3(°)		
0	0.0	9.138E-04	1.016	127.8	1.5	1.010	217.8	1.6	0.975	354.1	87.8	0.711	1.045
	5.0	9.261E-04	1.020	202.4	0.6	1.009	292.4	0.7	0.971	68.3	89.1	0.579	1.053
	10.0	9.320E-04	1.024	230.5	0.9	1.011	140.5	3.6	0.965	334.7	86.3	0.569	1.065
	15.0	9.504E-04	1.026	120.5	1.4	1.014	210.6	2.5	0.960	1.2	87.2	0.637	1.073
	22.5	9.461E-04	1.033	154.5	0.8	1.026	244.5	1.0	0.942	25.6	88.7	0.838	1.109
5	0.0	9.036E-04	1.018	2.5	5.1	1.006	272.2	4.2	0.976	143.4	83.4	0.411	1.044
	5.0	9.145E-04	1.020	17.9	2.3	1.013	108.1	4.7	0.968	262.3	84.8	0.717	1.059
	10.0	9.239E-04	1.026	244.7	2.3	1.015	334.7	0.6	0.959	78.6	87.6	0.653	1.075
	15.0	9.391E-04	1.026	165.5	0.6	1.017	75.4	5.1	0.958	262.6	84.9	0.733	1.077
	22.5	9.372E-04	1.033	71.5	2.5	1.024	161.5	1.5	0.942	283.6	87.1	0.802	1.107
10	0.0	8.683E-04	1.017	41.7	3.8	1.006	132.3	9.5	0.977	290.2	79.8	0.487	1.042
	5.0	8.810E-04	1.022	98.0	2.8	1.011	188.0	0.3	0.967	284.2	87.2	0.574	1.060
	10.0	8.887E-04	1.023	65.2	4.1	1.012	155.4	2.0	0.965	271.7	85.4	0.606	1.065
	15.0	9.071E-04	1.025	46.0	2.3	1.013	136.1	2.3	0.962	271.0	86.7	0.599	1.070
	22.5	9.028E-04	1.035	33.5	0.6	1.024	123.5	2.5	0.941	290.4	87.4	0.763	1.110
15	0.0	8.538E-04	1.014	309.8	6.6	1.003	217.6	19.0	0.984	58.1	69.9	0.275	1.031
	5.0	8.684E-04	1.022	141.7	0.1	1.005	231.7	5.0	0.973	50.5	85.0	0.307	1.051
	10.0	8.743E-04	1.023	344.6	1.6	1.011	254.4	7.2	0.966	87.0	82.7	0.552	1.062
	15.0	8.924E-04	1.024	209.0	3.0	1.017	299.2	3.1	0.960	75.4	85.6	0.780	1.074
	22.5	8.893E-04	1.032	168.3	0.1	1.026	258.3	3.6	0.942	76.1	86.4	0.875	1.107
20	0.0	8.173E-04	1.020	84.6	3.2	1.003	174.7	1.6	0.977	291.3	86.4	0.210	1.044
	5.0	8.302E-04	1.020	313.6	0.7	1.005	223.6	2.1	0.975	62.4	87.8	0.341	1.048
	10.0	8.357E-04	1.024	139.8	1.0	1.009	49.8	3.3	0.966	246.5	86.6	0.485	1.062
	15.0	8.546E-04	1.023	51.1	5.4	1.008	142.0	9.8	0.969	292.7	78.8	0.450	1.057
	22.5	8.492E-04	1.034	39.1	0.9	1.021	129.1	2.1	0.945	285.2	87.7	0.709	1.103

Supplementary Table 1(continued). c) Sample set C.

Porosity (%)	Compaction (%)	k_{Mean}	Maximum axis			Intermediate axis			Minimum axis			U	Pj
			K_1	D1(°)	I1(°)	K_2	D2(°)	I2(°)	K_3	D3(°)	I3(°)		
0	0.0	9.199E-04	1.022	264.5	6.0	1.002	354.6	0.7	0.975	91.3	84.0	0.178	1.048
	5.0	9.339E-04	1.022	244.1	1.3	1.007	334.2	2.9	0.970	129.5	86.8	0.435	1.055
	10.0	9.385E-04	1.024	228.1	1.6	1.013	318.2	2.8	0.962	109.4	86.8	0.642	1.069
	15.0	9.555E-04	1.025	79.0	0.1	1.013	349.0	0.6	0.961	179.6	89.4	0.618	1.072
	22.5	9.562E-04	1.038	273.7	2.7	1.021	3.8	0.3	0.939	100.2	87.3	0.65	1.113
5	0.0	9.039E-04	1.022	271.6	1.5	1.006	1.9	9.2	0.971	172.5	80.7	0.384	1.054
	5.0	9.181E-04	1.021	323.9	2.2	1.012	53.9	1.5	0.966	178.6	87.4	0.664	1.061
	10.0	9.246E-04	1.027	265.3	1.1	1.013	355.4	3.3	0.958	156.1	86.5	0.600	1.077
	15.0	9.411E-04	1.027	325.3	1.7	1.017	55.3	0.9	0.955	171.8	88.0	0.738	1.082
	22.5	9.409E-04	1.037	322.2	1.9	1.027	232.2	0.5	0.934	127.0	88.0	0.809	1.122
10	0.0	9.043E-04	1.018	43.6	4.1	1.008	313.5	2.6	0.973	191.3	85.1	0.594	1.049
	5.0	9.171E-04	1.021	133.9	0.8	1.010	43.9	3.2	0.968	238.6	86.7	0.593	1.058
	10.0	9.256E-04	1.027	122.2	1.1	1.015	32.1	4.6	0.956	225.5	85.3	0.671	1.080
	15.0	9.433E-04	1.029	287.1	1.3	1.012	17.2	3.8	0.957	178.7	86.0	0.537	1.079
	22.5	9.436E-04	1.037	331.4	0.6	1.029	61.4	2.9	0.932	230.2	87.0	0.861	1.126
15	0.0	8.679E-04	1.022	104.1	1.3	1.005	14.0	0.4	0.971	268.0	88.7	0.321	1.053
	5.0	8.818E-04	1.021	228.5	2.4	1.011	138.4	0.2	0.967	42.7	87.6	0.638	1.059
	10.0	8.882E-04	1.029	290.7	0.5	1.013	20.7	1.7	0.957	186.1	88.2	0.559	1.079
	15.0	9.029E-04	1.032	87.1	1.5	1.011	177.1	2.1	0.956	321.8	87.5	0.451	1.082
	22.5	9.023E-04	1.039	115.0	2.9	1.026	25.0	0.6	0.934	282.7	87.0	0.763	1.123
20	0.0	8.376E-04	1.016	337.9	5.4	1.006	68.1	2.1	0.977	179.4	84.2	0.494	1.042
	5.0	8.516E-04	1.022	231.9	1.4	1.009	322.0	3.5	0.968	119.8	86.3	0.511	1.059
	10.0	8.582E-04	1.027	348.0	2.7	1.013	257.9	1.9	0.959	132.8	86.7	0.595	1.075
	15.0	8.745E-04	1.027	270.5	0.5	1.014	0.5	2.6	0.957	169.1	87.4	0.633	1.079
	22.5	8.842E-04	1.034	104.3	0.6	1.034	14.3	2.8	0.931	206.7	87.2	0.985	1.129

Supplementary Table 1(continued). d) Sample set D.

Porosity (%)	Compaction (%)	k_{Mean}	Maximum axis			Intermediate axis			Minimum axis			U	Pj
			K_1	D1(°)	I1(°)	K_2	D2(°)	I2(°)	K_3	D3(°)	I3(°)		
0	0.0	9.160E-04	1.023	75.7	2.9	1.006	166.1	7.3	0.970	324.4	82.1	0.381	1.056
	5.0	9.280E-04	1.023	108.0	3.3	1.006	17.9	1.5	0.970	264.3	86.4	0.336	1.056
	10.0	9.360E-04	1.028	88.0	0.7	1.009	178.0	2.4	0.961	341.7	87.4	0.425	1.072
	15.0	9.540E-04	1.026	124.0	0.4	1.014	214.0	0.5	0.958	356.4	89.4	0.631	1.076
	22.5	9.510E-04	1.033	217.1	0.9	1.027	127.1	1.3	0.939	343.5	88.4	0.864	1.112
5	0.0	8.950E-04	1.019	46.4	1.6	1.007	316.3	3.1	0.973	163.7	86.5	0.473	1.049
	5.0	9.100E-04	1.022	310.5	0.7	1.012	40.5	0.5	0.965	165.7	89.1	0.636	1.063
	10.0	9.170E-04	1.024	10.2	3.6	1.017	100.3	2.2	0.958	221.7	85.7	0.784	1.076
	15.0	9.360E-04	1.030	235.3	2.0	1.016	325.3	1.1	0.952	84.1	87.7	0.635	1.087
	22.5	9.350E-04	1.040	324.7	0.1	1.025	54.7	3.0	0.933	232.1	87.0	0.731	1.125
10	0.0	8.890E-04	1.017	2.6	3.5	1.009	272.5	1.3	0.9727	162.1	86.3	0.622	1.050
	5.0	9.010E-04	1.020	352.9	4.9	1.014	262.7	2.8	0.964	143.0	84.3	0.796	1.064
	10.0	9.070E-04	1.027	13.5	0.9	1.014	103.5	0.7	0.958	234.0	88.9	0.629	1.077
	15.0	9.220E-04	1.029	113.2	1.2	1.014	23.1	4.8	0.956	217.4	85.0	0.575	1.081
	22.5	9.220E-04	1.038	291	0.1	1.024	21.0	1.9	0.936	199.0	88.1	0.731	1.119
15	0.0	8.630E-04	1.019	65.8	0.8	1.005	335.7	0.6	0.975	208.7	89.0	0.400	1.046
	5.0	8.750E-04	1.022	206.9	2.9	1.006	297.1	2.8	0.970	70.4	86.0	0.396	1.056
	10.0	8.800E-04	1.023	43.8	5.7	1.015	134.1	3.1	0.960	252.5	83.5	0.753	1.072
	15.0	8.960E-04	1.024	237.6	0.5	1.012	327.6	1.8	0.963	132.4	88.1	0.604	1.068
	22.5	8.950E-04	1.035	295.3	2.2	1.025	25.3	1.4	0.939	147.9	87.4	0.799	1.113
20	0.0	8.650E-04	1.019	302.8	3.4	1.006	32.9	1.1	0.973	140.4	86.5	0.447	1.049
	5.0	8.790E-04	1.021	307.0	1.7	1.008	37.0	2.0	0.970	176.4	87.4	0.481	1.054
	10.0	8.830E-04	1.024	42.1	1.1	1.013	132.1	0.8	0.963	256.4	88.7	0.635	1.069
	15.0	8.990E-04	1.026	313.6	5.8	1.013	223.2	3.8	0.959	99.8	83.1	0.589	1.074
	22.5	8.980E-04	1.037	312.0	0.4	1.020	222.0	1.4	0.942	59.4	88.5	0.643	1.108

1   **Suppl. Table 2: Summary of ARM shallowing as a function of compaction.** a) Sample set
2   A.

Porosity (%)	Compaction (%)	Intensity (*A/m*)	Declination (°)	Inclination (°)
0	0.0	3.34E-04	199.9	33.0
	10.0	3.31E-04	199.5	32.0
	22.5	3.16E-04	201.1	31.6
	30.0	3.13E-04	200.8	28.5
5	0.0	4.71E-04	153.9	41.9
	10.0	4.65E-04	153.2	40.0
	22.5	4.55E-04	153.2	38.4
	30.0	4.39E-04	151.9	37.5
10	0.0	4.28E-04	186.1	58.8
	10.0	4.13E-04	186.7	58.7
	22.5	3.91E-04	183.1	57.7
	30.0	3.75E-04	182.4	57.3
15	0.0	3.69E-04	212.8	44.4
	10.0	3.62E-04	212.8	43.7
	22.5	3.40E-04	215.6	43.0
	30.0	3.31E-04	216.5	42.4
20	0.0	2.59E-04	158.3	46.7
	10.0	2.52E-04	157.5	45.5
	22.5	2.41E-04	155.2	44.9
	30.0	2.22E-04	151.3	45.4

3
4

5   **Suppl. Table 2 (continued).**   b) Sample set B.
6

Porosity (%)	Compaction (%)	Intensity (*A/m*)	Declination (°)	Inclination (°)
0	0.0	4.09E-04	169.1	23.6
	10.0	4.08E-04	169.5	22.9
	15.0	4.06E-04	168.9	22.2
	22.5	4.05E-04	169.5	20.5
	30.0	4.03E-04	173.6	18.7
5	0.0	2.61E-04	164.8	36.3
	10.0	2.60E-04	161.4	35.1
	15.0	2.56E-04	160.8	34.2
	22.5	2.52E-04	163.3	33.4
	30.0	2.45E-04	163.1	29.7
10	0.0	2.46E-04	176.8	33.7
	10.0	2.45E-04	178.0	33.4
	15.0	2.42E-04	177.8	32.7
	22.5	2.38E-04	176.3	31.8
	30.0	2.33E-04	177.8	29.9
15	0.0	2.37E-04	187.8	39.6
	10.0	2.36E-04	185.8	39.3
	15.0	2.33E-04	185.6	39.0
	22.5	2.28E-04	184.9	37.2
	30.0	2.23E-04	186.2	36.7
20	0.0	3.67E-04	170.6	26.3
	10.0	3.66E-04	169.5	25.8
	15.0	3.63E-04	169.8	25.4
	22.5	3.59E-04	169.1	24.5
	30.0	3.53E-04	170.1	23.0

7
8

9   **Suppl. Table 2 (continued).** c) Sample set C.

10

Porosity (%)	Compaction (%)	Intensity (*A/m*)	Declination (°)	Inclination (°)
0	0.0	2.65E-04	198.4	46.8
	10.0	2.61E-04	199.0	45.5
	15.0	2.59E-04	198.9	44.5
	22.5	2.54E-04	198.1	42.5
	30.0	2.43E-04	199.7	38.4
5	0.0	2.59E-04	177.3	35.5
	10.0	2.56E-04	177.0	34.0
	15.0	2.54E-04	177.7	33.1
	22.5	2.51E-04	175.6	30.9
	30.0	2.43E-04	177.7	27.6
10	0.0	3.07E-04	177.2	20.6
	10.0	3.07E-04	177.4	20.5
	15.0	3.07E-04	177.6	19.6
	22.5	2.99E-04	178.1	17.5
	30.0	2.98E-04	179.7	14.7
15	0.0	2.29E-04	174.2	44.4
	10.0	2.27E-04	172.9	43.8
	15.0	2.23E-04	172.3	42.9
	22.5	2.14E-04	172.5	41.1
	30.0	2.10E-04	174.2	39.3
20	0.0	3.12E-04	207.3	34.2
	10.0	3.10E-04	207.5	33.6
	15.0	3.07E-04	207.6	33.0
	22.5	2.98E-04	208.4	30.5
	30.0	2.88E-04	208.5	27.5

11
12

13 **Suppl. Table 2 (continued).** d) Sample set D.

14

Porosity (%)	Compaction (%)	Intensity (*A/m*)	Declination (°)	Inclination (°)
0	0.0	3.92E-04	166.6	25.6
	10.0	3.91E-04	167.1	24.7
	15.0	3.91E-04	167.4	24.3
	22.5	3.87E-04	167.2	23.0
	30.0	3.80E-04	167.5	20.4
5	0.0	2.55E-04	147.6	41.0
	10.0	2.52E-04	147.7	39.9
	15.0	2.50E-04	147.5	39.0
	22.5	2.43E-04	146.9	37.3
	30.0	2.37E-04	150.4	34.3
10	0.0	2.83E-04	164.2	25.7
	10.0	2.80E-04	164.9	24.9
	15.0	2.82E-04	164.8	24.6
	22.5	2.78E-04	165.2	22.4
	30.0	2.75E-04	166.0	19.4
15	0.0	2.34E-04	193.8	36.4
	10.0	2.32E-04	194.9	35.7
	15.0	2.31E-04	193.6	35.1
	22.5	2.25E-04	193.7	33.5
	30.0	2.20E-04	195.4	31.8
20	0.0	3.83E-04	192.8	28.1
	10.0	3.83E-04	192.6	28.0
	15.0	3.81E-04	192.8	27.7
	22.5	3.76E-04	191.9	26.4
	30.0	3.66E-04	195.9	24.2

15
16
17
18